# Evaporative Crystallization in Drops on Superhydrophobic and Liquid-Impregnated Surfaces

Samantha A. McBride,[ID] Susmita Dash,[†] and Kripa K. Varanasi*[ID]

Department of Mechanical Engineering, Massachusetts Institute of Technology, 77 Massachusetts Avenue, Cambridge, Massachusetts 02139, United States

**Ⓢ** *Supporting Information*

**ABSTRACT:** Mineral-fouling induced corrosion and deterioration of marine vessels, aircraft, and coastal structures is due in part from structural intrusion of crystals grown from ocean-generated saline drops. As such, much work has explored surface treatments that induce hydrophobicity or introduce barriers for antifouling and corrosion prevention; however, the efficacy of these strategies will be altered by the underlying substrate texture. Here, we study the behavior of evaporating saline drops on superhydrophobic and liquid-impregnated surfaces as a function of surface texture. On superhydrophobic surfaces, four disparate regimes (which are not observed for particle-laden drops) emerge as a function of the substrate solid fraction: Cassie-pinning, Cassie-gliding, Cassie−Wenzel transition, and Wenzel. These regimes control the morphology of the resultant crystal deposits. In contrast to the superhydrophobic surfaces, spreading liquid-impregnated surfaces demonstrate minimal influence of solid fraction on evaporative crystallization. The area, area localization, timescale of evaporation, and deposit morphology are all normalized by the presence of the lubricating layer, thus introducing an efficient method of eliminating crystal "coffee rings" as well as reducing the potential for fouling and corrosion.
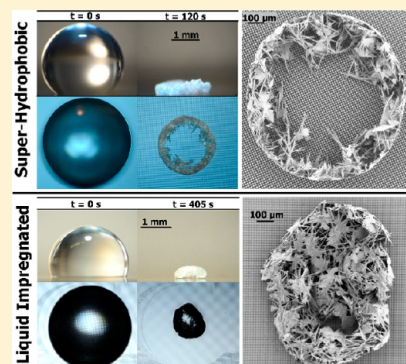
## INTRODUCTION

Evaporation of a particle-laden or saline drop on a substrate will generally leave behind either a ring,[1] a uniform deposit, or a condensed deposit. Ring deposits result from evaporative flow depositing particles at the drop contact line. These flows may be used for nanoseparations[2] or for self-assembly of electronics[3,4] and sensors.[5−7] Condensed deposits are favored for inkjet printing and result when particle deposition at the contact line is somehow disrupted. Such disruption can occur via addition of high-aspect-ratio particles,[8] use of a superhydrophobic substrate,[9,10] enhancement of the Marangoni effect,[11] heating of the substrate,[12] application of electric[13] or acoustic fields,[14] or via addition of certain polymers.[15−17]

Beyond technical interest in self-assembly and sensing, evaporative deposition from drops is pervasive and can lead to material degradation. Rain drops, spray from fast vehicles on wet roads, and ocean-generated aerosols are all examples in which particles/solutes may be deposited on surfaces. Costs associated with seaspray deposition run in billions of dollars[18,19] and primarily result from gypsum ($CaSO_4 \cdot 2H_2O$) formation on concrete and metallic structures.[20,21] Corrosion of structures occurs via surface mineral-fouling, cracking (in which crystals engrained in a crevice grow and apply pressure), and delamination.[20,22,23] This damage can sometimes be inhibited using hydrophobic coatings,[20,21] although such coatings face challenges regarding their temporal stability, environmental impacts,[24] and performance.[24,25]

While there are parallels between evaporation of saline drops and particle-laden drops, saline drops are somewhat more complicated. Concentration gradients are formed at the air/water interface as the volatile phase evaporates.[16] This heightened concentration combined with the predilection of crystals to form at interfaces results in crystal formation at the drop contact line.[26] Crystallization at the contact line will pin the drop and force a ring morphology even on surfaces that would normally form a clumped deposit for particle-laden systems.[17,27] The evolution of the crystals will alter drop pinning evaporation dynamics,[28] surface adhesion,[29] and the final form/size of the deposit. Therefore, eliminating coffee rings for crystal deposits remains a challenge despite the many approaches for eliminating coffee rings of colloidal deposits.

In this work, we explore crystallization from saline drops on three classes of a substrate: (1) hydrophilic, (2) superhydrophobic, and (3) liquid impregnated (Figure 1). Contact line pinning of drops on hydrophilic surfaces results in ring-shaped crystal deposits (Figure 1A). In previous investigations, both ring and condensed deposits have been observed on hydrophobic surfaces.[25,30] Ring patterns persist for gypsum deposits even on hydrophobic surfaces,[31] as the deposits depend not only on solid−liquid interactions but also on interactions between the salt and surface.[25,31] These
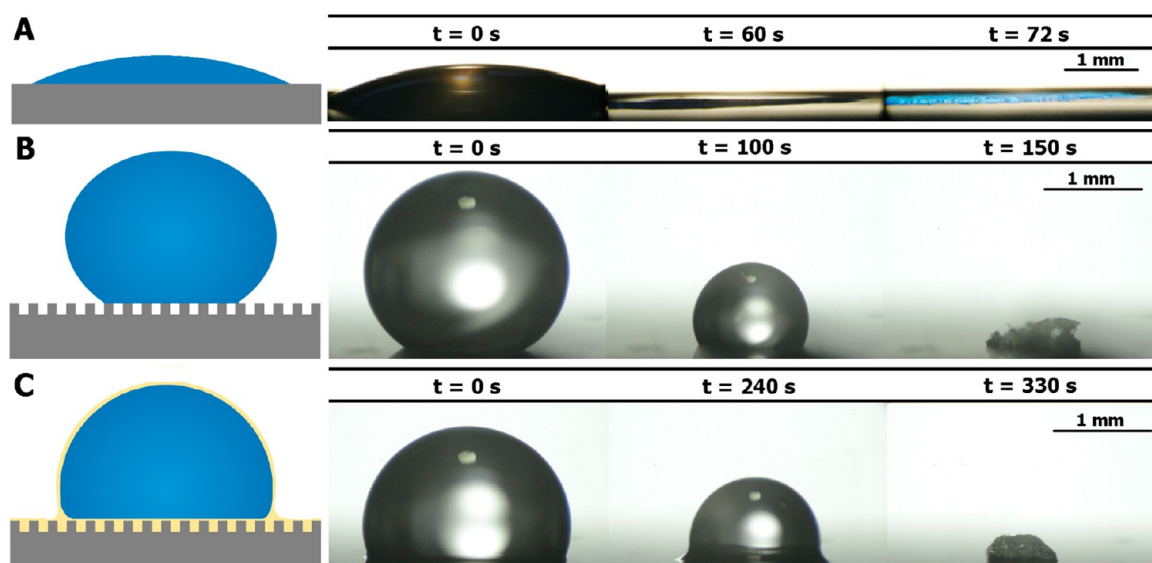
**Figure 1.** Schematics and images showing pinning behavior of evaporating calcium sulfate solution on (A) hydrophilic silicon (B) superhydrophobic microposts, and (C) a spreading liquid-impregnated surface (LIS). Images show the drops from both the top and side at three different times: (left) experiment initiation, (middle) shortly after crystallization has begun, and (right) end of evaporation.

interactions modify contact angle hysteresis of a surface, which then alters the evaporative deposits.[32] Superhydrophobic surfaces reduce contact-line pinning and should force formation of condensed deposits, as has been observed for colloids (Figure 1B).[33] However, we hypothesize that the formation of crystals will alter this behavior.

One strategy to prevent contact-line pinning and disrupt ring patterns is to use a liquid-impregnated surface (LIS, Figure 1C). These surfaces have a thin layer of a lubricating fluid impregnated within textures and have been previously demonstrated to minimize contact line pinning[34] and eliminate crystal fouling on surfaces.[35] By minimizing nucleation sites and adhesion between the burgeoning crystals and the solid substrate, LIS should avoid ring formation even for crystal deposits.

Here, we investigate evaporative gypsum crystallization from drops on superhydrophobic and liquid-impregnated micropost surfaces as a function of edge-to-edge post spacing, as a previous work has shown that geometric parameters of the posts have a strong influence on colloidal deposits.[9] We find that the surfaces most effective at preventing ring formation are those with low contact angle hysteresis that also remain stable in the Cassie state. We also validate the hypothesis that lubricant impregnation (using a fully spreading lubricant) of the micropost surfaces can suppress ring formation due to minimization of surface pinning (Figure 1C).[34,35] We confirm that lumped deposits form on the liquid-impregnated surfaces for all micropost geometries and thus introduce a new strategy for the disruption of ring formation from saline droplets.

## ■ MATERIALS AND METHODS

Photolithography using chrome masks (Advance Reproductions Corporations) was used to create arrays of square (10 $\mu$m wide) microposts with seven edge-to-edge post spacings: 5, 10, 25, 30, 40, 50, and 75 $\mu$m. The posts were etched to a height of 10 $\mu$m by reactive ion etch (Surface Technology Systems Inductively Coupled Reactive Ion Etch) at a pressure of 20 mTorr, rate of 500 nm/min, temperature of 40 °C, and coil power of 1200 W.[36,37] The photoresist was removed using Piranha solution, and the samples were further cleaned with acetone, isopropyl alcohol (IPA), and deionized (DI) water. The

surfaces were then rendered hydrophobic by coating them with octadecyltrichlorosilane (OTS, from Sigma-Aldrich) using liquid deposition by placing surfaces in 50 mL of toluene and adding 70 $\mu$L of OTS and 100 $\mu$L of DI water under sonication for 3 min. Any excess silane was removed through 2 min of sonication in an acetone bath, followed by additional rinses with acetone, IPA, and DI water. Silicone oil with a viscosity of 100 cSt was impregnated in the surfaces using a dipcoater (KSV Nima) to create the liquid-impregnated surfaces (LISs) without an excess film.[38] Saturated calcium sulfate solution was prepared by adding calcium sulfate dihydrate in excess to DI water, mixing over a period of several days, and filtering out undissolved solids.

Experiments were conducted by placing the test substrate on top of a plate heater maintained at 60 °C with a thin layer of thermal paste. Droplets of 5 $\mu$L saturated calcium sulfate solution were deposited on the substrate, and evaporation was recorded from both the top and side of the drops. Throughout these tests, the surrounding air was maintained at ambient conditions with a relative humidity range between 22 and 45%. Evaporation rates were not significantly influenced by differences in relative humidity, as heating at the substrate dominates the process (see the Supporting Information (SI) for analysis). The drop temperature is near that of the substrate and uniform, as the heat transfer timescale for 5 $\mu$L drops is between 5 and 10 s (see SI).[39,40] Control experiments at room temperature demonstrate that the elevated substrate/drop temperature does not significantly alter wetting regimes on the superhydrophobic surfaces (see SI).

Each experiment was repeated three to six times per substrate. High-resolution images of deposits were collected via a scanning electron microscope (SEM, Zeiss Supra5). Experimental movies were analyzed to find: (1) the contact angle ($\theta$) as a function of time, (2) the initial contact area of the drop ($A_o$), (3) the evaporation time ($t_E$), and (4) the final two-dimensional area of the crystal deposit ($A_c$).

Because pinning is essential for formation of ring-shaped deposits,[11] the area localization of deposits is a good predictor for deposit morphology. The area localization is defined as the ratio between the area covered by the final crystal deposit and the initial contact area of the drop ($A_c/A_o$). An area localization of ~1 suggests pinning of the contact line and therefore ring or uniform deposits, whereas smaller values suggest condensed deposits. Because formation of rings suggest pinning, ring deposits may be more strongly adhered to the surface; whereas clumped deposits form from a lack of pinning and therefore should be easier to remove.
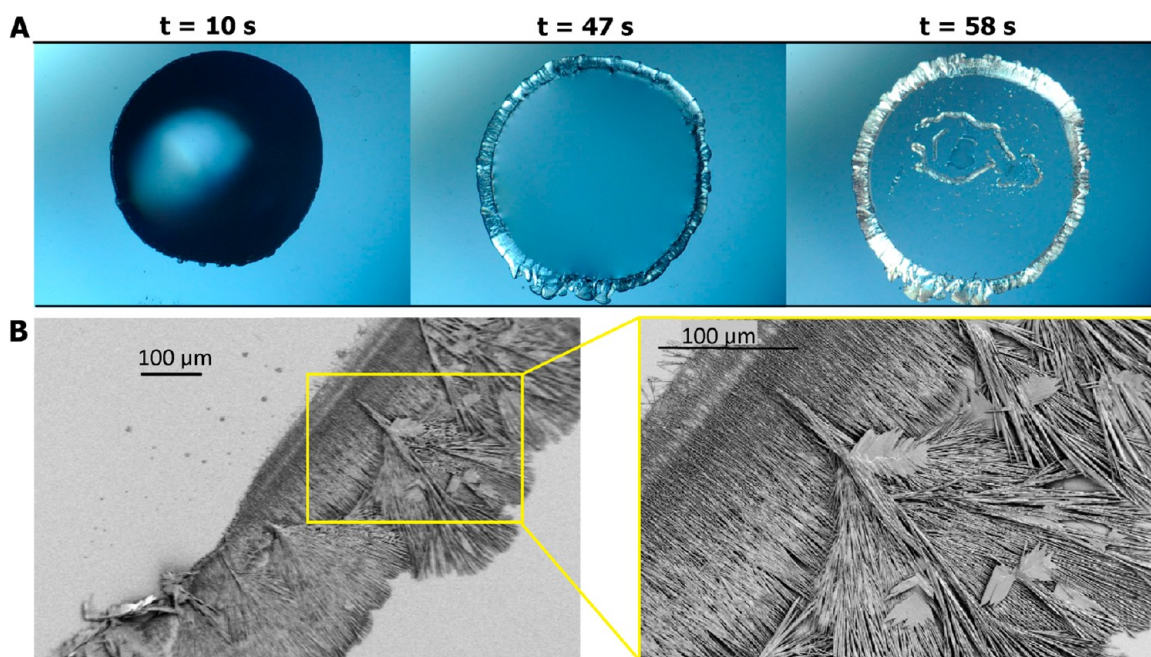
**Figure 2.** Evaporative crystallization on a hydrophilic silicon surface. (A) Progression of drop evaporation and crystal deposition. (B) SEM images from one deposit, showing dendritic needle-shaped gypsum crystals in plane with the substrate.

## ■ RESULTS AND DISCUSSION

Evaporation of sessile drops can proceed in either constant contact radius mode or in constant contact angle mode, with the former occurring for drops that have pinned to the surface. Evaporation on hydrophilic ($\theta = 24°$) silicon occurs in constant contact radius mode and results in the formation of ring-shaped deposits (Figure 2A). Crystallization initiates near the three-phase contact line approximately 10 s after drop deposition on the heated surface. The solution is then observed to wick into the precipitating crystals, further increasing the total footprint ($A_c/A_o = 1.09 \pm 0.30$) of the crystalline deposit. SEM images (Figure 2B) reveal needle-shaped crystals (a common structure for gypsum) oriented in the direction of the radial evaporative flow. These needles become thicker at the outer rim, likely due to the dramatic increase in flow velocity toward the end of evaporation.[41]

On a superhydrophobic surface with minimal contact angle hysteresis, sessile Cassie drop evaporation will generally occur in constant contact angle mode where the contact line continuously recedes, disrupting ring formation of colloidal deposits.[9] In contrast, we observed that evaporation of calcium sulfate solution results in crystallization at the triple-phase contact line, which can pin the contact line and change the evaporative mode to constant contact radius mode. This is seen in Figure 3A-i, which shows the progression of an evaporating drop of calcium sulfate solution on a superhydrophobic surface of 5 $\mu$m edge-to-edge spacing between posts (b5). The drop pins due to formation of crystals so that the final size of the deposit is similar to the contact area of the droplet ($A_c/A_o = 0.93$) and a ring deposit forms. However, this pinning is not observed for all of the micropost surfaces. Figure 3A-ii shows evaporation on the b25 surface, in which the contact line recedes before pinning occurs and more condensed deposits ($A_c/A_o = 0.68$) result.

In total, four regimes are observed for evaporative crystallization on superhydrophobic post surfaces. First, there is the pinning regime where ring deposits form, as seen in the case of the b5 surface (Figure 3A). As post spacing increases (b10, b25, and b30), evaporation begins in a constant contact angle mode, with the drop sliding over the posts to form condensed deposits ($A_c/A_o = 0.69$ for b10, 0.68 for b25, and 0.74 for b30). In the third regime, drops are initially suspended in the Cassie state but transition to the Wenzel state (Figure 3A-iii). This transition causes a double ring deposit (seen most clearly on the b50 SEM image of Figure 3C) and a large area localization ($A_c/A_o = 1.5$ for b40, 2.72 for b50). The fourth and final regime is observed in the case of the b75 surface, in which drops evaporate in constant contact radius mode in the Wenzel state to form a simple ring deposit.

The disparate crystal pattern regimes across the different post surfaces can be rationalized by differences in contact angle and contact angle hysteresis. A surface with a large contact angle hysteresis will evaporate in constant contact radius mode until the contact angle reduces to the receding angle. A drop on a low-hysteresis surface (with a receding angle similar to the advancing angle) will begin receding shortly after onset of evaporation. Hence, we predict that saline droplets evaporating on a surface with a higher hysteresis will become pinned by emerging crystals before receding begins. In contrast, drops on low-hysteresis surfaces will recede before crystals can form and pin the contact line.

For the micropost surfaces used here, the contact angle hysteresis decreases with decreasing solid fraction while drops are suspended in the Cassie state (Table S1, Supporting Information).[42] The b5 surface has the largest solid fraction and highest contact angle hysteresis of the Cassie surfaces, resulting in crystals pinning the contact line into the ring shape before the drop begins to recede from evaporation. The b10, b25, and b30 surfaces have lower hysteresis and recede significantly prior to crystallization, resulting in the clumped deposits observed in the constant contact angle regime. Differences between the deposit morphologies and individual crystal structures for these surfaces (seen in SEM images for b10, b25, and b30 of Figure
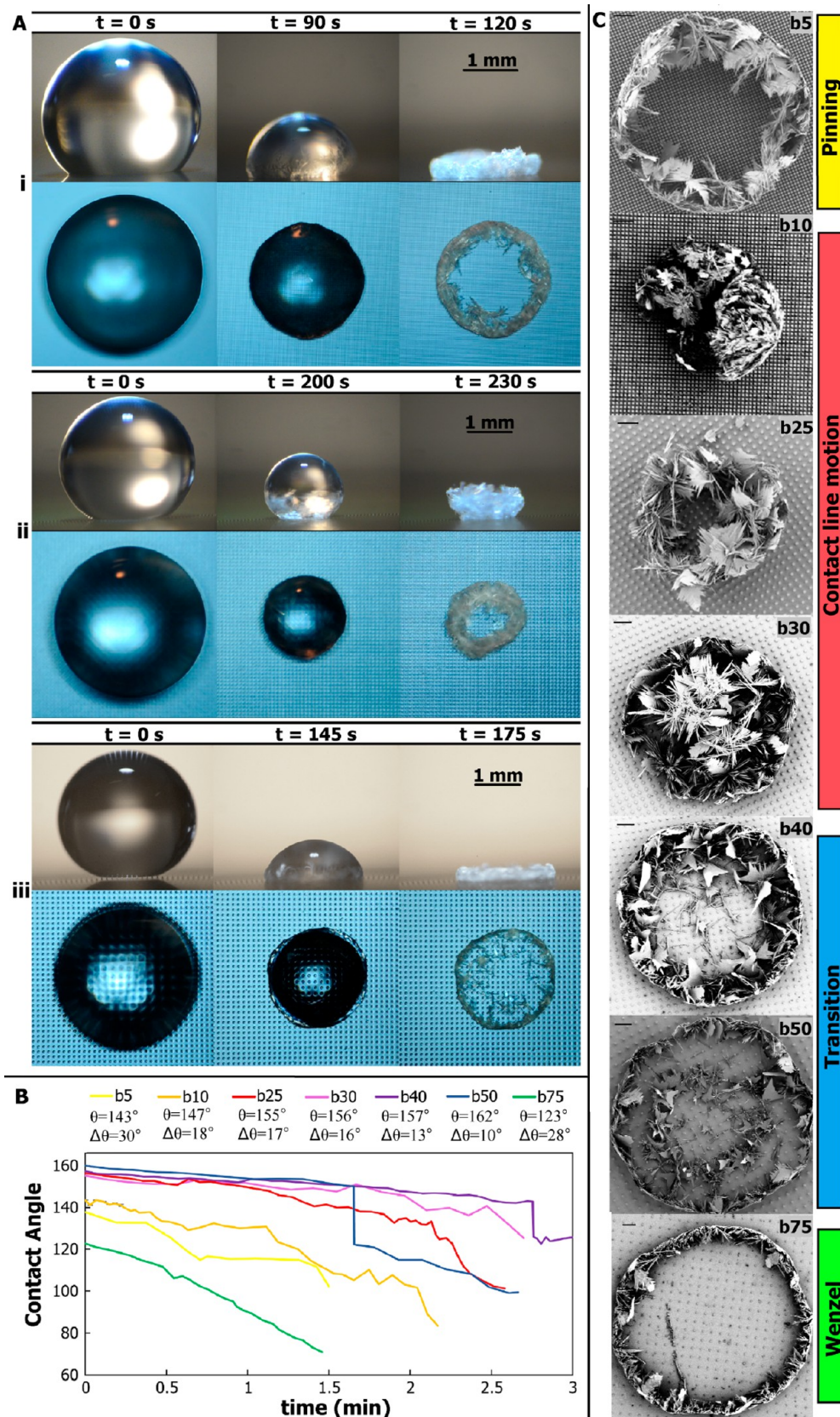
**Figure 3.** (A) Representative examples of evaporative crystallization on superhydrophobic micropost surfaces with edge-to-edge post spacing of (i) 5, (ii) 25, and (iii) 50 $\mu$m. The images show the top and side views of drops at three different time instants: (left) experiment initiation, (middle) shortly after crystals at triple-phase contact line have pinned the drop, and (right) end of evaporation. (B) Contact angle as a function of time throughout evaporation (until crystal deposits obscure measurements). (C) SEM images of crystalline deposits. Scale bars represent 100 $\mu$m.
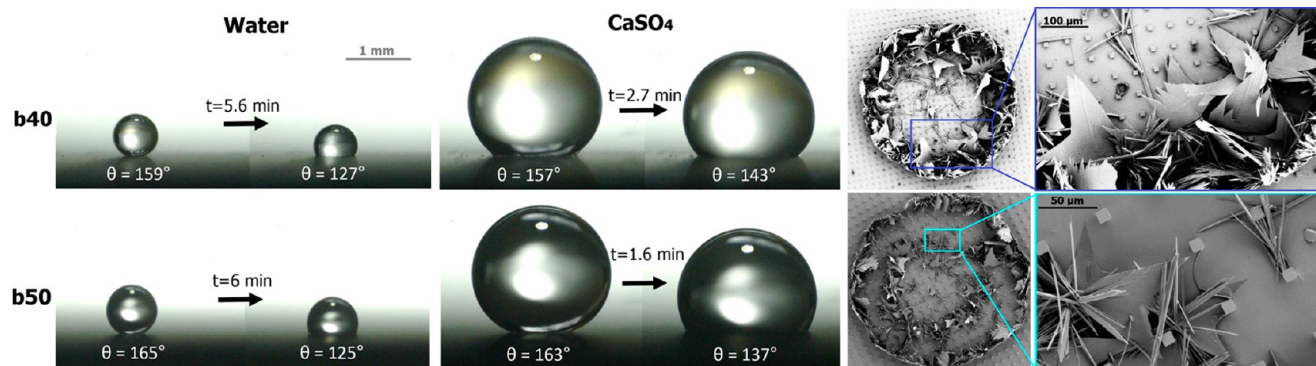
**Figure 4.** Comparing the b40 and b50 Cassie to Wenzel transitions for water to those for calcium sulfate solution. SEM images show crystal growth on posts.

3C) can be attributed to the inherent stochasticity of crystallization.

As crystallization impacts the contact angle hysteresis, it also changes the evaporation dynamics and total evaporation time as a result. Figure 3B shows contact angle as a function of time, with measurements terminated at the point at which the crystal deposit became prominent enough that no contact angle could be accurately determined. Moving from b5 (yellow line) to b40 (pink line), we see an increase in the initial contact angle with a corresponding increase in the evaporation time. This trend is due to high-contact-angle surfaces having a lowered rate of heat transfer from the heated surface to the drops.[42,43] However, the trend is disrupted by the Cassie to Wenzel transition. The transition on the b50 surface occurs much earlier than it does on the b40 surface because of reduced stability of the Cassie state on the b50 surface. The drop on the b50 surface evaporates faster than the one on the b40 surface because it spends more time in the Wenzel state, which has a higher rate of heat transfer than that in the Cassie state.[43]

The dynamics of drop evaporation and formation of salt crystals are interdependent. For example, we see that evaporation time decreases due to the presence of the calcium sulfate in water (see the SI for data). This result may seem at odds with the known decrease in saturation vapor pressure of evaporating saline water, but the saturation concentration of calcium sulfate in water is low enough such that neither the saturation vapor pressure nor the colligative properties of water are strongly altered by its presence (see the SI). The change in evaporation time here is instead caused by contact line pinning due to crystallization, forcing the drop into constant radius mode and thereby increasing the surface area and evaporation rate. The overall deposit shape is readily explainable by the contact angle, hysteresis, and presence/absence of the transition. However, the morphologies of crystals are also varied between the deposits, as seen in the SEM images of Figure 3C. Faster evaporation concentrates salt rapidly and increases supersaturation, which causes faster nucleation and smaller crystals. In contrast, crystals grown from slower processes at lower supersaturation levels will be larger and exhibit fewer defects.[44] This is qualitatively observed in Figure 3C, where deposits with slower evaporation times tend to have large, leaflike crystals and fewer overall crystals, whereas deposits formed by faster evaporation tend to have a larger number of overall crystals, many of which are thin needles.

The transition from the Cassie to Wenzel state observed for drops on the b40 and b50 surfaces is expected, as the Cassie state is metastable for these surfaces.[45] To further probe the

dynamics of this transition and the influence of crystallization, control experiments using DI water were conducted (Figure 4, see also the SI). For the DI water drops, evaporation of the 5 μL volume drops proceeds for 5.6 min on the b40 surface and for 6 min on the b50 surface prior to transition. This is contrasted by the evaporation of the 5 μL drops of saturated calcium sulfate solution, which transition to the Wenzel state after 2.7 min on the b40 and 1.6 min on the b50 surface. Although one may expect this is due to a difference in surface tension caused by the presence of solute, the low solubility concentration of calcium sulfate does not result in significant deviations from the surface tension of DI water.[31,46] Instead, the enhancement in transition time is due to formation of crystals (which are hydrophilic) within the texture, leading to drop impalement, as opposed to the typical Laplace pressure-driven transitions for DI water. This phenomenon is confirmed by the existence of the interior ring of the "double ring" structure of the b50 surface (see Figure 4), which provides clear evidence that crystals form on the texture at the Cassie contact line prior to impalement. The water will preferentially wet the hydrophilic crystals at the air/water interface, causing a decrease in the Cassie angle and a consequent transition to the Wenzel state. Control experiments confirm that the ratio of the transition time to the total evaporation time remains relatively constant at a range of temperatures for both water ($t_{trans}/t_{evap} = 0.95$) and calcium sulfate ($t_{trans}/t_{evap} = 0.66-0.77$), further demonstrating that transition is driven by super-saturation and precipitation, as opposed to pressure effects from evaporation (see Table S4 and Figure S3 in the SI).

Despite the promise of superhydrophobic post surfaces in preventing formation of ring deposits, crystallization at the surface still causes contact line pinning. Therefore, we performed experiments using liquid-impregnated surfaces (LISs) with the same micropost morphology as the super-hydrophobic surfaces to reduce contact line pinning (Figure 5). LISs are textured substrates impregnated with a liquid.[34,47−49] These surfaces can eliminate crystallization on the textures by reducing pinning of the drop to the surface. A system composed of a drop on top of an LIS can exist in 12 possible thermodynamic states dictated by the droplet, impregnating lubricant, and texture.[34] For stability, the lubricant−substrate contact angle must be less than the critical angle $\theta_C = \cos^{-1}(1 - \varphi)/(r - \varphi)$, where $\varphi$ is the solid fraction and $r$ is the substrate roughness.[38] The state of the lubricant impregnated within the textures is dictated by the spreading coefficient ($S_{LS(W)} = \gamma_{SW} - \gamma_{LS} - \gamma_{LW}$, where $\gamma$ is interfacial energy between the phases) of the lubricant (L) on the substrate (S) in the presence of the
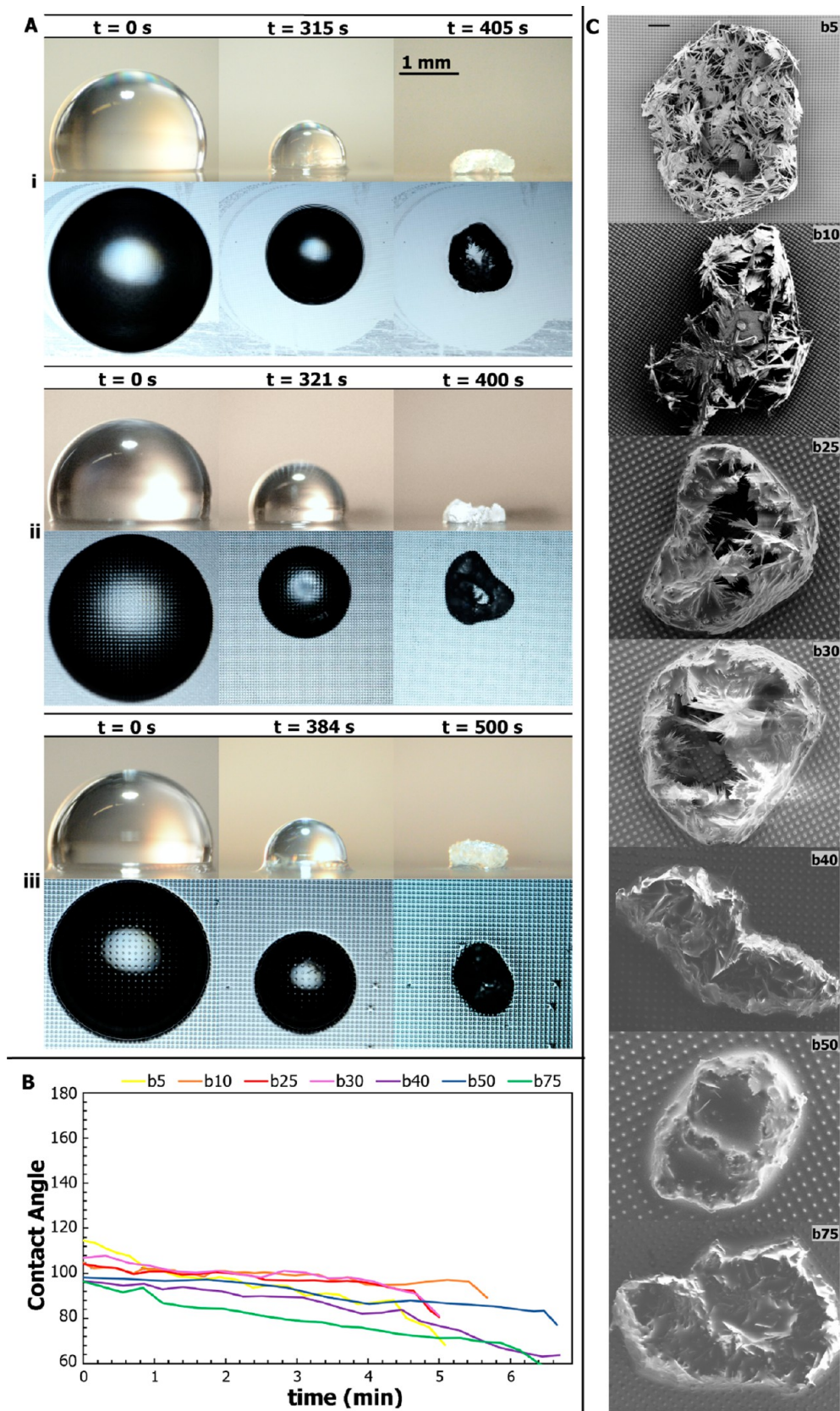
**Figure 5.** (A) Progression of evaporative crystallization on liquid-impregnated surfaces of (i) b5, (ii) b25, and (iii) b50. Top and side view images are shown for three time instants: (left) experiment onset, (middle) shortly after crystals become apparent, and (right) end of evaporation. (B) Contact angle as a function of time for LISs, with measurements terminated after crystal deposits become too prominent for accurate measurement. (C) SEM images showing crystal deposits on the different LISs. Scale bar represents 100 $\mu$m and is the same for all images.
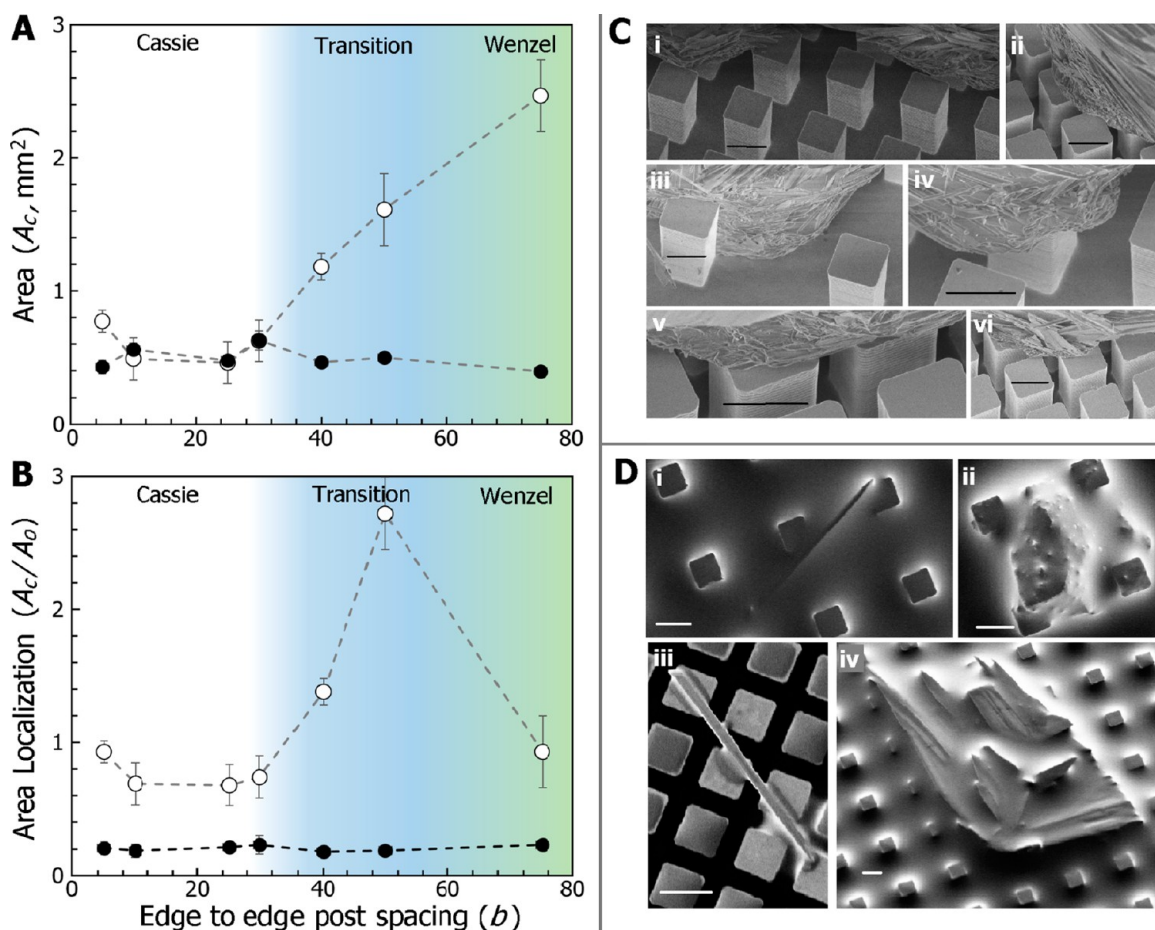
**Figure 6.** Comparison of evaporation behavior on the (○) superhydrophobic and (●) liquid-impregnated surfaces as functions of substrate pitch. (A) The total area of deposits; (B) area Localization, the ratio of the area of the final crystal deposit to the initial footprint of the drop; (C) points of pinning on Cassie superhydrophobic post surfaces with many small crystals: (i) crystals formed on b10 posts, (ii) crystals covering b5 posts, (iii) crystals that have engulfed a b50 post, (iv) pinning crystals that have engulfed the top of a b10 post, and (v, vi) close up of crystals on b5 posts. Scale bars represent 10 $\mu$m; (D) crystals left over after removing deposits from LISs as follow: (i) needlelike crystal that has fallen into the oil between posts on a b25 surface, (ii) chunk of a crystal stuck between posts on b25, (iii) needlelike crystal deposited on top of b5 LIS posts, and (iv) large leaflike crystal deposited on top of b25 posts. Scale bars represent 10 $\mu$m.

droplet (W). When $S_{LS(W)} > 0$, the lubricant completely spreads on the texture and creates a barrier between the drop and the surface. When $S_{LS(W)} < 0$, the tops of the texture remain emerged and dictate the pinning of the droplet.[34] On the basis of previous results that have shown crystal formation atop the textures on a nonspreading LIS ($S_{LS(W)} < 0$), here, we focus on spreading LIS ($S_{LS(W)} > 0$).[35] In addition, a thin layer of the oil cloaks the droplet as the spreading coefficient of oil on the water droplet in the presence of air is positive ($S_{LW(A)} > 0$, as illustrated in the schematic of Figure 1C).

Figure 5A shows the progression of drop evaporation on liquid-impregnated b5, b25, and b50 surfaces, respectively. Unlike the superhydrophobic surfaces, disparate regimes are not observed. Instead, drop evaporation occurs in near-constant contact angle mode throughout the entire period of evaporation on all surfaces with varying textures (Figure 5B). The drops on LIS continue to shrink in size even after the first signs of crystallization are observed, in contrast to the drops on superhydrophobic substrates that were pinned by emerging crystals. Evidence of this lack of pinning is clear from the b25 LIS progression (Figure 5A-ii), where the drop has migrated toward the top of the field of view even while crystals begin to form. Lack of contact line pinning results in a complete absence

of the ring-shaped structures observed on the hydrophilic and superhydrophobic surfaces.

The lack of contact line pinning on LIS results in highly condensed deposits, which are composed of relatively large crystals (Figure 5C). We observe that oil can wick into the crystal deposit, consistent with a previous investigation where oil from LIS wicked into frost deposits.[50] In the SEM images of Figure 5C, this creates an appearance of "smoothness", as the sharp crystal formations are covered by oil wicked into the scale deposit. The degree of oil migration into the crystals is dictated by the relative balance between capillary wicking of the crystal deposit and the underlying texture. Denser textures (b5, b10) retain oil more readily when compared to sparser textures (b30–b75).

In addition to the lack of dependence of deposit morphology across different texture regimes, LIS also reduces variations in the timescale of evaporation (Figure 5B). Whereas super-hydrophobic surfaces demonstrated disparate evaporation timescales, evaporation on the LIS is nearly constant across the surfaces.

The differences between evaporative deposition of crystals on the superhydrophobic surfaces and LIS are reflected in the overall deposit size (Figure 6A) and the area localization

(Figure 6B) as a function of the substrate solid fraction. For the superhydrophobic surfaces, the deposit area has a clear trend with the texture dependent on the wetting state, whereas the deposit area is independent of texture on LIS. The deposits on the superhydrophobic surfaces in the "Cassie-gliding" regime have contact area similar to that of the deposits on LIS; however, the area localization is significantly lower on the liquid-impregnated surfaces due to constant contact angle evaporation ($A_c/A_o = 0.68$ for superhydrophobic, 0.2 for LIS, Figure 6B).

Figure 6C shows a variety of examples of pinning points across different superhydrophobic post surfaces. These pinning points comprise of many small crystals, suggesting a large amount of crystal nucleation in these areas. Crystal nucleation occurs readily in the presence of surfaces containing imperfections that can serve as nucleation sites or that can lower the energy barrier for nucleation.[51] Hydrophobic coatings increase the energy barrier for nucleation at the surface, yet it is clear that crystals are still able to find nucleation sites on the posts. This is contrasted by the deposits left behind on the LISs (Figure 6D), where only large crystals that are not pinned to the posts are observed. Because of the lubricating layer, these large crystals were highly mobile and easily removed by rinsing with saturated calcium sulfate solution.

## CONCLUSIONS

We investigated the role of contact line pinning on deposit morphology from evaporating saline drops using super-hydrophobic and liquid-impregnated micropost surfaces with varying solid fractions. We show that the formation of ring-shaped crystalline deposits on superhydrophobic surfaces can be disrupted by tuning the solid fraction to ensure evaporation occurs in the Cassie-gliding regime. This ideal regime contains surfaces with solid fractions that minimize contact angle hysteresis while also remaining stable to Cassie–Wenzel transitions. Unlike superhydrophobic surfaces, experiments on spreading liquid-impregnated surfaces were invariable to the solid fraction due to the presence of an oil layer preventing both nucleation and pinning of crystals at the surface. Hence, LIS can serve as an efficient antifouling surface to prevent seaspray deposition and resulting corrosion. These results also introduce new strategies for controlling crystalline deposits and for disrupting the coffee-ring effect, which has proven to be more difficult for crystals than for colloids. The delayed onset of crystallization on LIS may also allow for new approaches of growing large, well-defined crystals as well as for concentrating dilute solutions of valuable materials such as difficult-to-synthesize pharmaceuticals.

## ASSOCIATED CONTENT

### ⓢ Supporting Information

The Supporting Information is available free of charge on the ACS Publications website at DOI: 10.1021/acs.langmuir.8b00049.

> Calculation for the theoretical wetting angles for both the Cassie and Wenzel states as a function of the surface solid fraction, static contact angle measurements from experiments, advancing and receding contact angles, a brief note on the nucleation of crystals at surfaces; analysis of colligative properties and the evaporation differences between water and calcium sulfate solution; data from control experiments performed on the superhydrophobic surfaces at room temperature, controls exploring the influence of temperature on the Cassie–Wenzel transition on the superhydrophobic b50 surface, and modeling of the evaporative timescales and influence of relative humidity, convection, and heat transfer (PDF)

## AUTHOR INFORMATION

### Corresponding Author

*E-mail: Varanasi@mit.edu.

### ORCID ⓘ

Samantha A. McBride: 0000-0002-6402-1359
Kripa K. Varanasi: 0000-0002-6846-152X

### Present Address

†Department of Mechanical Engineering, Indian Institute of Science, CV Raman Road, Bangalore, India, 560012.

### Author Contributions

The manuscript was written through contributions of all authors. S.A.M., S.D., and K.K.V. designed the research. S.A.M. performed research. S.A.M., S.D., and K.K.V. analyzed the data. S.A.M. wrote the draft manuscript. S.A.M., S.D., and K.K.V. edited and wrote the final manuscript.

## REFERENCES

(1) Deegan, R. D.; Bakajin, O.; Dupont, T. F.; Huber, G.; Nagel, S. R.; Witten, T. A. Capillary Flow as the Cause of Ring Stains from Dried Liquid Drops. *Nature* **1997**, *389*, 827−829.

(2) Wong, T.-S.; Chen, T.-H.; Shen, X.; Ho, C.-M. Nano-chromatography Driven by the Coffee Ring Effect. *Anal. Chem.* **2011**, *83*, 1871−1873.

(3) Magdassi, S.; Grouchko, M.; Toker, D.; Kamyshny, A.; Balberg, I.; Millo, O. Ring Stain Effect at Room Temperature in Silver Nanoparticles Yields High Electrical Conductivity. *Langmuir* **2005**, *21*, 10264−10267.

(4) Liu, L.; Ma, S.; Pei, Y.; Xiong, X.; Sivakumar, P.; Singler, T. J. Regulation of the Deposition Morphology of Inkjet-Printed Crystalline Materials via Polydopamine Functional Coatings for Highly Uniform and Electrically Conductive Patterns. *ACS Appl. Mater. Interfaces* **2016**, *8*, 21750−21761.

(5) Malfatti, L.; Tokudome, Y.; Okada, K.; Yagi, S.; Takahashi, M.; Innocenzi, P. Coffee Stain-Driven Self-Assembly of Mesoporous Rings. *Microporous Mesoporous Mater.* **2012**, *163*, 356−362.

(6) Wen, J. T.; Ho, C.-M.; Lillehoj, P. B. Coffee Ring Aptasensor for Rapid Protein Detection. *Langmuir* **2013**, *29*, 8440−8446.

(7) Esmonde-White, K. A.; Esmonde-White, F. W. L.; Morris, M. D.; Roessler, B. J. Characterization of Biofluids Prepared by Sessile Drop Formation. *Analyst* **2014**, *139*, 2734−2741.

(8) Yunker, P. J.; Still, T.; Lohr, M. A.; Yodh, A. G. Suppression of the Coffee-Ring Effect by Shape-Dependent Capillary Interactions. *Nature* **2011**, *476*, 308−311.

(9) Dicuangco, M.; Dash, S.; Weibel, J. A.; Garimella, S. V. Effect of Superhydrophobic Surface Morphology on Evaporative Deposition Patterns. *Appl. Phys. Lett.* **2014**, *104*, No. 201604.

(10) Cui, L.; Zhang, J.; Zhang, X.; Li, Y.; Wang, Z.; Gao, H.; Wang, T.; Zhu, S.; Yu, H.; Yang, B. Avoiding Coffee Ring Structure Based on Hydrophobic Silicon Pillar Arrays during Single-Drop Evaporation. *Soft Matter* **2012**, *8*, 10448−10456.

(11) Hua, H.; Larson, R. G. Marangoni Effect Reverses Coffee-Ring Depositions. *J. Phys. Chem. B* **2006**, *110*, 7090−7094.

(12) Li, Y.; Yang, Q.; Li, M.; Song, Y. Rate-Dependent Interface Capture beyond the Coffee-Ring Effect. *Sci. Rep.* **2016**, *6*, No. 24628.

(13) Eral, H. B.; Augustine, D. M.; Duits, M. H. G.; Mugele, F. Suppressing the Coffee Stain Effect: How to Control Colloidal Self-Assembly in Evaporating Drops Using Electrowetting. *Soft Matter* **2011**, *7*, 4954−4958.

(14) Mampallil, D.; Reboud, J.; Wilson, R.; Wylie, D.; Klug, D. R.; Cooper, J. M. Acoustic Suppression of the Coffee-Ring Effect. *Soft Matter* **2015**, *11*, 7207−7213.

(15) Seo, C.; Jang, D.; Chae, J.; Shin, S. Altering the Coffee-Ring Effect by Adding a Surfactant-like Viscous Polymer Solution. *Sci. Rep.* **2017**, *7*, No. 500.

(16) Li, F.-I.; Thaler, S. M.; Leo, P. H.; Barnard, J. A. Periodic Pattern Formation in Evaporating Drops. *J. Phys. Chem. B* **2006**, *110*, 25838−25843.

(17) Kaya, D.; Belyi, V. A.; Muthukumar, M. Pattern Formation in Drying Droplets of Polyelectrolyte and Salt. *J. Chem. Phys.* **2010**, *133*, No. 114905.

(18) Sastri, V. S. Corrosion Costs. *Challenges in Corrosion*; John Wiley & Sons, Inc: Hoboken, 2015; pp 95−126.

(19) Amani, M.; Hjeij, D. *A Comprehensive Review of Corrosion and Its Inhibition in the Oil and Gas Industry*; Society of Petroleum Engineers, 2015; pp 1−14.

(20) Doehne, E. Salt Weathering: A Selective Review. In *Natural Stone, Weathering Phenomena, Conservation Strategies and Case Studies*; Siegard, S., Siegard, S., Weiss, T., Vollbrecht, A., Eds.; The Geological Society, 2001; pp 51−64.

(21) Scherer, G. W.; Flatt, R.; Wheeler, G. Materials Science Research for the Conservation of Sculpture and Monuments. *MRS Bull.* **2001**, *26*, 44−50.

(22) Scherer, G. W. Crystallization in Pores. *Cem. Concr. Res.* **1999**, *29*, 1347−1358.

(23) Desarnaud, J.; Bonn, D.; Shahidzadeh, N. The Pressure Induced by Salt Crystallization in Confinement. *Sci. Rep.* **2016**, *6*, No. 30856.

(24) Doehne, E.; Price, C. A. *Stone Conservation: An Overview of Current Research*, 2nd ed.; Getty Publications: Los Angeles, CA, 2010.

(25) Shahidzadeh-Bonn, N.; Rafai, S.; Bonn, D.; Wegdam, G. Salt Crystallization during Evaporation: Impact of Interfacial Properties. *Langmuir* **2008**, *24*, 8599−8605.

(26) Accardo, A.; Burghammer, M.; Cola, E. D.; Reynolds, M.; Fabrizio, E. D.; Riekel, C. Calcium Carbonate Mineralization: X-Ray Microdiffraction Probing of the Interface of an Evaporating Drop on a Superhydrophobic Surface. *Langmuir* **2011**, *27*, 8216−8222.

(27) Diao, Y.; Myerson, A. S.; Hatton, T. A.; Trout, B. L. Surface Design for Controlled Crystallization: The Role of Surface Chemistry and Nanoscale Pores in Heterogeneous Nucleation. *Langmuir* **2011**, *27*, 5324−5334.

(28) Soulié, V.; Karpitschka, S.; Lequien, F.; Prené, P.; Zemb, T.; Moehwald, H.; Riegler, H. The Evaporation Behavior of Sessile Droplets from Aqueous Saline Solutions. *Phys. Chem. Chem. Phys.* **2015**, *17*, 22296−22303.

(29) Accardo, A.; Mecarini, F.; Leoncini, M.; Brandi, F.; Cola, E. D.; Burghammer, M.; Riekel, C.; Fabrizio, E. D. Fast, Active Droplet Interaction: Coalescence and Reactive Mixing Controlled by Electro-wetting on a Superhydrophobic Surface. *Lab Chip* **2013**, *13*, 332−335.

(30) Shin, B.; Moon, M.-W.; Kim, H.-Y. Rings, Igloos, and Pebbles of Salt Formed by Drying Saline Drops. *Langmuir* **2014**, *30*, 12837−12842.

(31) Shahidzadeh, N.; Schut, M. F. L.; Desarnaud, J.; Prat, M.; Bonn, D. Salt Stains from Evaporating Droplets. *Sci. Rep.* **2015**, *5*, No. 10335.

(32) Eral, H. B.; 't Mannetje, D. J. C. M.; Oh, J. M. Contact Angle Hysteresis: A Review of Fundamentals and Applications. *Colloid Polym. Sci.* **2013**, *291*, 247−260.

(33) Zhang, J.; Borg, M. K.; Sefiane, K.; Reese, J. M. Wetting and Evaporation of Salt-Water Nanodroplets: A Molecular Dynamics Investigation. *Phys. Rev. E* **2015**, *92*, No. 052403.

(34) Smith, J. D.; Dhiman, R.; Anand, S.; Reza-Garduno, E.; Cohen, R. E.; McKinley, G. H.; Varanasi, K. K. Droplet Mobility on Lubricant-Impregnated Surfaces. *Soft Matter* **2013**, *9*, 1772−1780.

(35) Subramanyam, S. B.; Azimi, G.; Varanasi, K. K. Designing Lubricant-Impregnated Textured Surfaces to Resist Scale Formation. *Adv. Mater. Interfaces* **2014**, *1*, No. 1300068.

(36) Subramanyam, S. B.; Rykaczewski, K.; Varanasi, K. K. Ice Adhesion on Lubricant-Impregnated Textured Surfaces. *Langmuir* **2013**, *29*, 13414−13418.

(37) Dorrer, C.; Rühe, J. Wetting of Silicon Nanograss: From Superhydrophilic to Superhydrophobic Surfaces. *Adv. Mater.* **2008**, *20*, 159−163.

(38) Seiwert, J.; Clanet, C.; Quere, D. Coating of a Textured Solid. *J. Fluid Mech.* **2011**, *669*, 55−63.

(39) Gambaryan-Roisman, T. Solid Substrate Properties. *Droplet Wetting Evaporation*; Elsevier, 2015; Chapter 11, pp 139−156.

(40) Hays, R. C. *Thermal Transport to Sessile Water Droplets on Heated Superhydrophobic Surfaces of Varying Cavity Fraction*; Brigham Young University, 2013.

(41) Marín, Á. G.; Gelderblom, H.; Lohse, D.; Snoeijer, J. H. Order-to-Disorder Transition in Ring-Shaped Colloidal Stains. *Phys. Rev. Lett.* **2011**, *107*, No. 085502.

(42) Chen, X.; Ma, R.; Li, J.; Hao, C.; Guo, W.; Luk, B. L.; Li, S. C.; Yao, S.; Wang, Z. Evaporation of Droplets on Superhydrophobic Surfaces: Surface Roughness and Small Droplet Size Effects. *Phys. Rev. Lett.* **2012**, *109*, No. 116101.

(43) Dash, S.; Garimella, S. V. Droplet Evaporation on Heated Hydrophobic and Superhydrophobic Surfaces. *Phys. Rev. E* **2014**, *89*, No. 042402.

(44) Mullin, J. W. *Crystallization*, 4th ed.; Butterworth-Heinemann, 2001.

(45) Patankar, N. A. On the Modeling of Hydrophobic Contact Angles on Rough Surfaces. *Langmuir* **2003**, *19*, 1249−1253.

(46) Ferron, G. A.; Soderholm, S. C. Estimation of the Times for Evaporation of Pure Water Droplets and for Stabilization of Salt Solution Particles. *J. Aerosol Sci.* **1990**, *21*, 415−429.

(47) Quéré, D. Non-Sticking Drops. *Rep. Prog. Phys.* **2005**, *68*, 2495−2532.

(48) Wong, T.-S.; Kang, S. H.; Tang, S. K. Y.; Smythe, E. J.; Hatton, B. D.; Grinthal, A.; Aizenberg, J. Bioinspired Self-Repairing Slippery Surfaces with Pressure-Stable Omniphobicity. *Nature* **2011**, *477*, 443−447.

(49) Schellenberger, F.; Xie, J.; Encinas, N.; Hardy, A.; Klapper, M.; Papadopoulos, P.; Butt, H.-J.; Vollmer, D. Direct Observation of Drops on Slippery Lubricant-Infused Surfaces. *Soft Matter* **2015**, *11*, 7617−7626.

(50) Rykaczewski, K.; Anand, S.; Subramanyam, S. B.; Varanasi, K. K. Mechanism of Frost Formation on Lubricant-Impregnated Surfaces. *Langmuir* **2013**, *29*, 5230−5238.

(51) Russell, K. C. Nucleation in Solids: The Induction and Steady State Effects. *Adv. Colloid Interface Sci.* **1980**, *13*, 205−318.